Applied Catalysis B: Environment and Energy 351 (2024) 123968

Contents lists available at ScienceDirect

Applied Catalysis B: Environment and Energy

journal homepage: www.elsevier.com/locate/apcatb

Oxygen vacancies-rich Co_3O_4 cones loaded low content Pd for efficient and fast electrocatalytic hydrodechlorination

Tao Li, Zhenyu Kong, Maomao Liu, Yuanyuan Sun, Lipeng Diao, Ping Lu, Daohao Li *, Dongjiang Yang *

State Key Laboratory of Bio-fibers and Eco-textiles, College of Environmental Science and Engineering, College of Materials Science and Engineering, Qingdao University, Qingdao 266071, PR China

ARTICLE INFO

Keywords:
Electrocatalytic hydrodechlorination
Chlorinated organic compounds
Pd electrocatalyst
Oxygen vacancy
Co_3O_4

ABSTRACT

Pd-based materials have been considered to be the preferred electrocatalysts for electrocatalytic hydrodechlorination (EHDC) due to their excellent H* production capacity. However, the scarcity and high price of Pd restrict its use, thus, an efficient Pd-based EHDC electrocatalyst with low Pd content should be developed. In this work, oxygen vacancies-rich Co_3O_4 ($Co_3O_{4\text{-}OV}$) cone-like architecture growth in situ on Ni foam was used as an intermediate layer to synthesize Pd@$Co_3O_{4\text{-}OV}$/NF EHDC electrocatalyst with low Pd loading (0.0254 mg cm^{-2}). Pd@$Co_3O_{4\text{-}OV}$/NF electrocatalyst can obviously promote the H* production and shows high EHDC activity with a dechlorination activity (DA) of 2.07 $mmol_{2,4\text{-}DCP}$ g_{Pd}^{-1} min^{-1} for EHDC of 2,4-dichlorophenol, which is higher than most reported Pd-modified electrodes. The Pd@$Co_3O_{4\text{-}OV}$/NF exhibited excellent anti-background interference ability (different initial pH and anions in aqueous solution) and good cycle stability (5 consecutive EHDC cycles), which could effectively improve aquatic biosafety.

1. Introduction

Chlorinated organic compounds (COCs) have found extensive use in various fields such as insecticides, electronics, chemical manufacturing, petroleum refining, and medicines [1,2]. However, the majority of COCs are extremely toxic, bioaccumulative, and resistant to degradation, which might cause substantial environmental issues as well as damage to human health [3,4]. Different methods have been exploited for the or removal of COCs, including biodegradation [5,6], physical treatment [7,8], photocatalysis [9,10], and electrocatalytic hydrodechlorination (EHDC) [11–13]. Among them, EHDC treatment has been proposed as one of the most promising methods with the features of high efficiency, gentle reaction conditions, and low apparatus cost [14,15].

EHDC is an indirect reduction reaction pathway launched by the active atomic hydrogen (H*), which is created in situ on the surface of specific cathode materials via H^+ reduction [16]. H* acts as potent reducing species for the breakage of carbon-chlorine (C-Cl) bonds of COCs to reduce toxicity by hydrodechlorination [17]. So far, Pd-based materials have excellent H* production capacity, which are considered to be preferred electrocatalysts for EHDC [18]. Nevertheless, significant expenses and limited deposits of Pd pose constraints on its large-scale practical application in water treatment. Therefore, it is necessary to design a reasonable Pd structure to obtain excellent electrochemical performance while reducing the amount of Pd.

A reduction in the loading of Pd on the catalyst often results in a drop in hydrodechlorination activity, particularly in terms of reaction rate. Seeking a suitable intermediate layer as the support of Pd can effectively reduce the Pd loading and keep high EHDC activity. Transition metal oxides (TMOs) have garnered significant attention as potential candidates for electrocatalysis owing to their advantageous attributes such as cost effectiveness, abundant reserves, and exceptional electrochemical stability [19]. Thus, it is reasonable to design TMOs-based Pd electrocatalyst because the water dissociation (Volmer step, $H_2O + * + e^- \rightarrow H^* + OH^-$) property of TMOs is beneficial to generate H* for EHDC reaction. However, TMOs suffer from inefficient water splitting kinetics due to low conductivity and low exposed active site [20]. According to previous researches, introducing oxygen vacancies to TMOs has been found to remarkably boost electrical conductivity and reactivity of active sites, thus enhancing water splitting activity [21,22]. The promoted H* production capacity is effective for tuning the reaction kinetics and speeding up the reaction rate. Meanwhile, oxygen vacancies on TMOs-support can serve as the anchoring points to catch and load Pd by

* Corresponding authors.
E-mail addresses: lidaohao@qdu.edu.cn (D. Li), d.yang@qdu.edu.cn (D. Yang).

https://doi.org/10.1016/j.apcatb.2024.123968
Received 12 September 2023; Received in revised form 19 January 2024; Accepted 15 March 2024
Available online 16 March 2024

strong metal−support interactions (SMSI), which is advantageous to reduce Pd loading and improve atomic utilization [23]. Furthermore, the SMSI effect can regulate the electronic environment of loaded Pd atoms by redistributing the charge between the TMOs-support and the Pd, leading to enhancement of adsorption and activation of substrate molecules, which is conducive to efficient and fast EHDC reaction [24].

In this work, oxygen vacancies-rich Co_3O_4 ($Co_3O_{4\text{-}OV}$) cone-like architecture growth in situ on Ni foam (NF) was used as an intermediate layer to synthesize Pd@$Co_3O_{4\text{-}OV}$/NF EHDC electrode with low Pd loading (0.0254 mg cm^{-2}). SMSI effect between $Co_3O_{4\text{-}OV}$/NF support and Pd can induce electrons to transfer from the $Co_3O_{4\text{-}OV}$/NF support to the Pd active sites, which promotes water splitting and EHDC reaction. The prepared Pd@$Co_3O_{4\text{-}OV}$/NF can obviously promote the H* production and shows high EHDC activity with a dechlorination activity (DA) of 2.07 $mmol_{2,4\text{-}DCP}$ g_{Pd}^{-1} min^{-1} for EHDC of 2,4-dichlorophenol (2,4-DCP), which is higher than most reported Pd modified electrodes. Meanwhile, the material has good adaptability in the water environment of different initial pH (3−11) solutions and different anions (4 mM NO_3^-, NO_2^-, Cl^-, CO_3^{2-}) and has good cycle stability by repeating the EHDC reaction for five consecutive cycles. Finally, by testing the activity of Chlorella cells in different predetermined solutions, the improvement of biosafety in water after EHDC treatment is proved.

2. Experimental

2.1. Chemicals and materials

Cobalt nitrate ($Co(NO_3)_2$ 6 H_2O, AR), urea ($CO(NH_2)_2$, AR), ammonium fluoride (NH_4F, GR), tert-butanol (t-BuOH, AR), acetone (AR), hydrochloric acid (HCl, AR), Sodium borohydride ($NaBH_4$, AR), 5,5-dimethyl-1-pyrroline N-oxide ($C_6H_{11}NO$, DMPO, 97%), and ethanol absolute (AR) were supplied by Chemical reagents of Sinopharm Group. 2,4-Dichlorophenol (2,4-DCP, >98.0%), phenol (P, AR), o-Chlorophenol (o-CP, 99.0%), 4-Chlorophenol (p-CP, 98.0%), 2-Fluorophenol (≥98.0%), 2-Bromophenol (98.0%), 2,4-Dichlorbenzoic acid (2,4-DCBA, 98.0%), 2,4-Dichlorophenoxyacetic acid (2,4-D, 97.0%), Chloramphenicol (CAP, 98.0%), sodium sulfate anhydrous (Na_2SO_4, AR), and palladium (II) chloride ($PdCl_2$, ≥99.0%) were purchased from Aladdin Reagent Co., Ltd., China. All solutions were made with ultrapure water (specific conductivity ≥18.2 mΩ cm^{-1}). Suzhou Sinero Technology Co., Ltd supplied the Ni foam (pore density=110ppi) used in this work. DuPont provided the cation exchange membrane (Nafion-117) used in this study.

2.2. Synthesis of $Co_3O_{4\text{-}OV}$/NF

Before fabrication, the Ni foam (1.5*1.5 cm^2) was successively cleaned in acetone, HCl solution (3 M), ethanol absolute and ultrapure water with ultrasonication for 10 min respectively and then dried in a vacuum oven for 6 hours at 60 ℃. The interference factors, such as oxide layer and organic carbon on the surface can be removed by pretreatment.

The components of the supported solution of Co_3O_4 were NH_4F (3 mmol), urea (7 mmol), $Co(NO_3)_2{\cdot}6\ H_2O$ (2 mmol), and ultrapure water (30 mL), which were mixed evenly at room temperature. The clean Ni foam and mixed solution were added to a 50 mL polytetrafluoroethylene autoclave and then heated at 130 ℃ for 4 hours. The obtained samples were dried in a vacuum oven at 60 ℃ for 6 hours. Subsequently, the samples were then put in a tube furnace and heated to 350 °C for 2 hours at a ramping rate of 2 ℃/min in the air atmosphere to obtain Co_3O_4/NF. The Co_3O_4/NF was soaked in 0.75 M $NaBH_4$ solution for 2 hours to get $Co_3O_{4\text{-}OV}$/NF.

2.3. Synthesis of Pd@$Co_3O_{4\text{-}OV}$/NF

The $Co_3O_{4\text{-}OV}$/NF was put into the precursor solution of ultrapure water (24 mL) and 1 mL $PdCl_2$ aqueous solution (10 mM; $PdCl_2$ dissolved in HCl solution to form $PdCl_4^{2-}$, n($PdCl_2$): n(HCl)=1:2), and then irradiated by the ultraviolet light (UV, 365 nm, 15 W*4) for 60 min to load Pd.

For comparison, Pd@NF, Pd@Co_3O_4/NF were prepared by the same method.

2.4. Electrochemical test measurements

Reductive EHDC experiments of 2,4-DCP were carried out in a traditional H-type two-chamber cell. The anode and cathode chamber cells were separated by a Nafion-117 membrane. The cathode chamber comprised 40 mL aqueous solution containing Na_2SO_4 (50 mM) and 2,4-DCP (80 mg L^{-1}), while the anode chamber comprised 40 mL Na_2SO_4 (50 mM) solution. The prepared electrodes mentioned were used as the cathode electrode, and a platinum sheet (1.5*1.5 cm^2) and an Ag/AgCl electrode were used as the anode electrode and reference electrode, respectively. The solution in cathode chamber and anode chamber was saturated with N_2 before testing. The electrolyte of cathode chamber was magnetically stirred during electrolysis. The constant current was 10 mA cm^{-2}, and the working time was 2 hours at room temperature. 0.5 mL of sample was taken from the cathode chamber at certain intervals and filtered by a 0.45 μm filter for high-performance liquid chromatography (HPLC) analysis, the mobile phase contained 70% methanol and 30% water and the flow rate was 1.0 mL min^{-1}. The dechloridation efficiency of 2,4-DCP was calculated as: CE (%) = (1 - C_t/C_0) ×100%, where C_t is the concentration of 2,4-DCP at time t, C_0 is the initial 2,4-DCP concentration. A pseudo-first-order kinetics model was used to describe the reaction and expressed as: Ln (C_t / C_0) = - K × t, where K is the apparent rate constant (min^{-1}) obtained from a linear regression of ln (C_t / C_0) versus t. The dechlorination activity (DA) of Pd was calculated under optimal conditions based on the quantity of reactants converted: DA = N_0 × α / (M_{Pd} × t), where N_0 represents the moles of initial 2,4-DCP (mmol), M_{Pd} is the total Pd loading (g), α represents the conversion of 2,4-DCP (α = 50%), and t is the electrolysis time (min).

2.5. Material characterization

The crystal structure of samples was analysed by DX2700 X-ray diffraction (XRD, Dandong, China) with a Cu Kα radiation (λ=1.5418 Å), operating at 40 kV voltage and 30 mA current. The morphology and structure of the samples were investigated by an FEI Magellan 400 field emission scanning electron microscope (FESEM) and a JEOL JEM-2100 F scanning transmission electron microscope (STEM) equipped with Cs probe corrector at 200 kV. X-ray photoelectron spectroscopy (XPS) was measured by Thermo Scientific K-Alpha XPS with Al Ka radiation (hv=1486.6 eV). Inductively coupled plasma (ICP) was performed using Agilent 7800 to determine the loading of Pd on Pd@$Co_3O_{4\text{-}OV}$/NF. Electron spin resonance spectroscopy (ESR) was performed to determine the main active species (H*) in EHDC by Bruker EMXnano. Linear sweep voltammetry (LSV) was carried out on CHI760e electrochemical workstation. EHDC experiments were conducted on multichannel electrochemical analyser (Iviumn stat, Netherlands). The concentrations of the different pollutants were monitored by HPLC (Dalian ELITE, China), utilizing a UV–VIS detector at 275 nm with a C18 column (4.6×150 mm, 5μm). The optical density (OD) of the healthy Chlorella cells was measured by using a UV−vis spectrophotometer (Persee T9s) at 680 nm.

3. Results and discussion

3.1. Synthesis and characterization

Fig. 1a illustrates the synthesis procedure of the Pd@$Co_3O_{4\text{-}OV}$/NF. Firstly, the Co_3O_4/NF was synthesized by hydrothermal method at 130

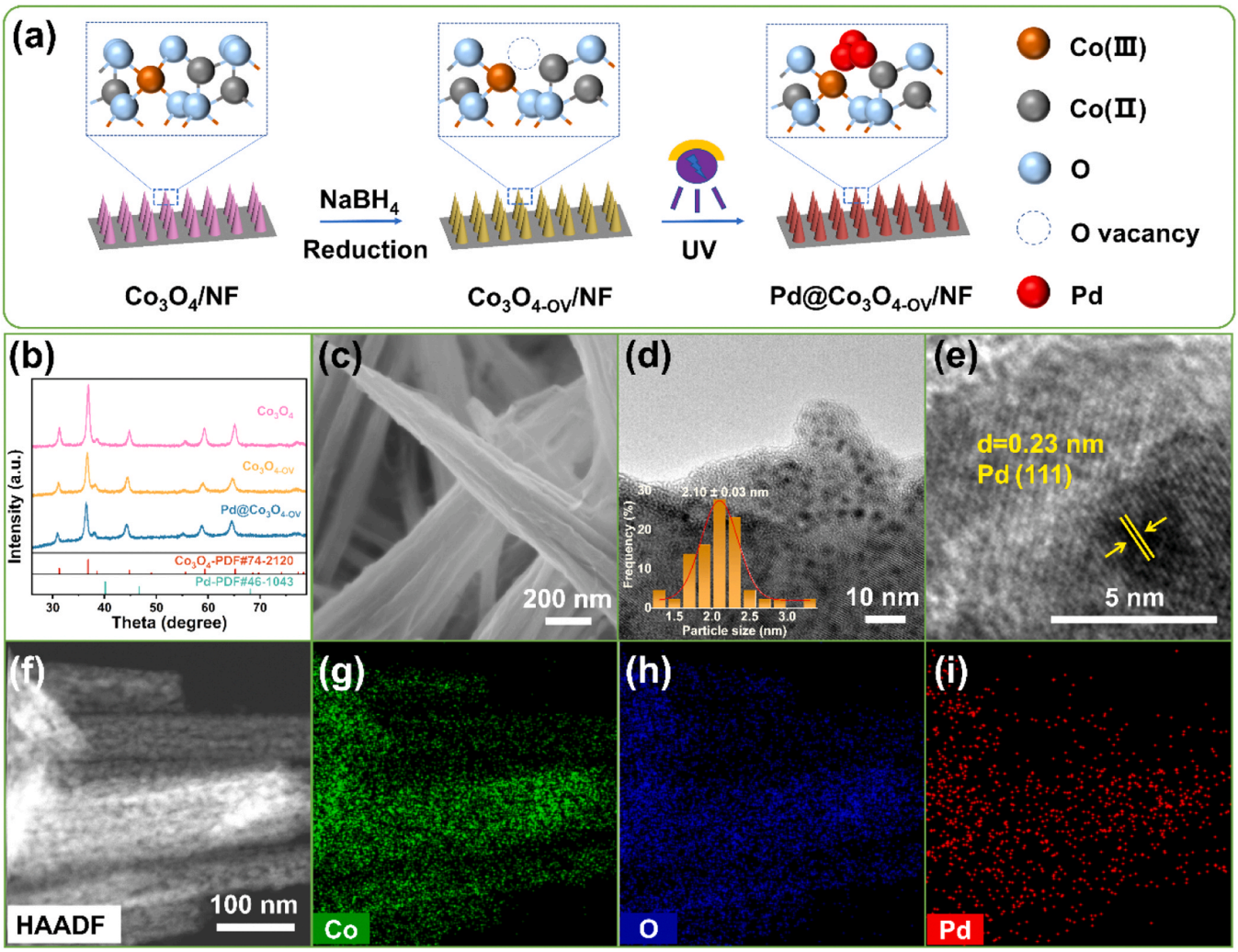

Fig. 1. (a) Synthesis diagram of Pd@$Co_3O_{4\text{-}OV}$/NF electrocatalyst; (b) XRD patterns of Co_3O_4, $Co_3O_{4\text{-}OV}$ and Pd@$Co_3O_{4\text{-}OV}$ powders; (c) SEM image of Pd@$Co_3O_{4\text{-}OV}$/NF electrocatalyst; (d) TEM image of Pd@$Co_3O_{4\text{-}OV}$/NF electrocatalyst (inset: the corresponding Pd size distribution); (e) HRTEM image of Pd@$Co_3O_{4\text{-}OV}$/NF electrocatalyst; (f-i) EDS mapping images of the Pd@$Co_3O_{4\text{-}OV}$/NF.

℃ for 4 hours and then calcined in air at 350 ℃ for 2 hours. The $Co_3O_{4\text{-}OV}$/NF material, which has a high concentration of oxygen vacancies, was synthesized by immersing Co_3O_4/NF in a 0.75 M $NaBH_4$ solution for a duration of 2 hours [25]. An ultraviolet reduction method was used to load Pd on the $Co_3O_{4\text{-}OV}$/NF [26,27]. The $Co_3O_{4\text{-}OV}$/NF was fully soaked in Pd^{2+} precursor solution to allow the Pd^{2+} to be adsorbed in its oxygen vacancies and then irradiated by UV (ultraviolet light) to obtain Pd@$Co_3O_{4\text{-}OV}$/NF.

The X-ray diffraction (XRD) patterns of Co_3O_4 exhibit distinct peaks at certain angles, namely 31.3°, 36.9°, 38.6°, 44.8°, 55.6°, 59.3°, and 65.2°. These peaks may be attributed to the crystallographic planes (220), (311), (222), (400), (422), (511), and (440) of Co_3O_4, as shown by the JCPDS#74–2120 (Fig. 1b). Particularly, the XRD pattern of $Co_3O_{4\text{-}OV}$ is similar to Co_3O_4, indicating that the crystalline phase of Co_3O_4 remains unchanged after $NaBH_4$ reduction [28]. However, the XRD pattern peaks intensity of $Co_3O_{4\text{-}OV}$ sample and Pd@$Co_3O_{4\text{-}OV}$ sample are lower than that of Co_3O_4 sample, indicating the crystallinity of Co_3O_4 is reduced after $NaBH_4$ reduction. The amount of Pd loading was 0.0254 mg cm^{-2} within Pd@$Co_3O_{4\text{-}OV}$/NF sample (examined by inductively coupled plasma). The XRD pattern does not exhibit any further distinctive peaks following the introduction of Pd, which potentially related to a low Pd loading. Fig. S1 shows that bare NF has a smooth surface. The propensity for Pd to aggregate can readily result in formation of Pd agglomerates on the surface of electrocatalyst [29]. For Pd@NF, spherical Pd clusters are dispersedly formed on the surface of NF (Fig. S2). The large-sized clusters may reduce the EHDC performance and stability of Pd catalysts due to active site blockage. The surface morphology of $Co_3O_{4\text{-}OV}$/NF is observed in Fig. S3. Large, dense Co_3O_4 cones directly cover the surface of macroporous nickel foam, considerably increasing the surface area of the electrocatalyst, which is conducive to full contact of the electrode with the electrolyte. The lattice fringes observed in the image, with respective spacing distances of 0.202 and 0.282 nm, may be attributed to the (400) and (220) crystallographic planes of the Co_3O_4 phase in spinel structure (Fig. S4) [30,31]. The surface morphology (SEM) of Pd@$Co_3O_{4\text{-}OV}$/NF is similar to $Co_3O_{4\text{-}OV}$/NF, and no obvious Pd clusters are observed on it after Pd loading, indicating the low loading and good dispersion of Pd (Fig. 1c). The TEM image and the relevant Pd size distribution show the Pd nanoparticles with a mean diameter of about 2.10 nm uniformly dispersed on the $Co_3O_{4\text{-}OV}$/NF support (Fig. 1d). The average size of the Pd structure in Pd@$Co_3O_{4\text{-}OV}$/NF is slightly smaller than that in Pd@Co_3O_4/NF. Fig. S5 shows the aggregation of Pd nanoparticles with a mean diameter of about 2.49 nm on the Co_3O_4/NF support was relatively concentrated, and the dispersion effect is general. The anion vacancies on the surface of the $Co_3O_{4\text{-}OV}$/NF support will lead to more exposure to Pd^{2+} adsorption sites, which promotes the dispersion of Pd. The high-resolution transmission electron microscopy (HRTEM) picture indicates a lattice spacing of 0.23 nm, which corresponds well with the

(111) plane of the Pd nanoparticles (Fig. 1e) [32]. The energy dispersive spectrometry (EDS) mapping analysis of Pd@$Co_3O_{4\text{-}OV}$/NF demonstrates a homogeneous dispersion of Co, O, and Pd elements (Fig. 1f-i).

X-ray photoelectron spectroscopy (XPS) was used to better comprehend the local composition information of prepared samples (Fig. 2 and S6). The XPS spectra of all samples have prominent signals corresponding to Co and O elements. The spectrum of C1s can be neglected because of the adsorbed CO_2 in the air [33]. The XPS spectra of Pd@Co_3O_4/NF and Pd@$Co_3O_{4\text{-}OV}$/NF reveal two new minuscule peaks at approximately 337 and 342 eV that are attributed to Pd 3d, which suggests the successful introduction of Pd (Fig. 2a and S6a) [34]. The XPS spectrum of Co 2p exhibits two distinct peaks at 794.70 and 779.60 eV, which may be attributed to Co^{3+} $2p_{1/2}$ and Co^{3+} $2p_{3/2}$ states, respectively. Additionally, the peaks seen at 796.20 and 781.10 eV can be ascribed to Co^{2+} $2p_{1/2}$ and Co^{2+} $2p_{3/2}$ states, respectively (Fig. 2b and S6b) [35]. The three shake-up satellites (abbreviated 'Sat') of Co 2p are typical peaks of the Co_3O_4 material [36]. By comparing the area covered by the fitting contours, it is feasible to determine the Co^{2+}/Co^{3+} relative atomic ratio on Co_3O_4/NF and $Co_3O_{4\text{-}OV}$/NF surface. Clearly, the Co^{2+}/Co^{3+} atomic ratio of $Co_3O_{4\text{-}OV}$/NF (2.84) is greater than that of Co_3O_4/NF (1.65), indicating that a fraction of Co^{3+} ions are reduced to Co^{2+} ions on the surface of Co_3O_4/NF in conjunction with the generation of oxygen vacancies following $NaBH_4$ reduction [37]. The formation of oxygen vacancies results in a decrease in the binding energies of Co. The confirmation of oxygen vacancies may be further supported by analyzing the O 1 s spectra (Fig. 2c). The O 1 s XPS spectra were fitted to obtain obvious characteristic peaks located at 529.68, 531.28, 532.68, and 535.48 eV, corresponding to typical metal-oxygen bond (O_L), oxygen vacancies (O_V), hydroxyl or surface-adsorbed oxygen (O_{ads}) and adsorbed water (O_W) (Fig. 2c and S6c) [38–41]. The SMSI between Pd and metal oxides will significantly enhance the adsorption of surface oxygen-containing species (O_{ads} and O_W), which is advantageous for the production of active H* on the Pd surface to promote EHDC [42]. The area percentage of O_V covered by the fitting curves can be obtained from the XPS spectra. It is obvious that the O_V area percentage of the $Co_3O_{4\text{-}OV}$/NF (44.21%) is significantly higher than that of Co_3O_4/NF (28.78%). The results indicate that the Co_3O_4/NF material prepared by high-temperature annealing contains a certain amount of oxygen vacancies, which will increase considerably after treatment with $NaBH_4$, and oxygen vacancy sites on Co_3O_4/NF serve as active sites for stabilizing and reducing Pd^{2+} to Pd [43,44]. The two peaks located at 342.57 and 337.27 eV are considered to be Pd^0 $3d_{3/2}$ and Pd^0 $3d_{5/2}$, and the others at 343.81 and 338.55 eV are considered to be Pd^{2+} $3d_{3/2}$ and Pd^{2+} $3d_{5/2}$, indicating the coexistence of Pd^0 (major) and Pd^{2+} species (Fig. 2d) [45,46]. After Pd loading, the peaks of Co 2p binding energy on Pd@$Co_3O_{4\text{-}OV}$/NF show positive shifts, which are greater than those of Pd@Co_3O_4/NF (Fig. 2b and S6b). Moreover, Compared with Pd@Co_3O_4/NF, a lager positive shift of the O_L binding energy is observed on Pd@$Co_3O_{4\text{-}OV}$/NF after Pd anchoring (Fig. 2c and S6c). Electrons transferred from the Co_3O_4 interlayer to Pd, thus leaving Pd in an electron-rich state. Fig. 2d shows that the peaks of Pd 3d binding energy loaded on the oxygen vacancies-rich $Co_3O_{4\text{-}OV}$/NF support negatively shift relative to Pd@Co_3O_4/NF, which indicates that Pd obtains more electrons from the vacancies-rich $Co_3O_{4\text{-}OV}$/NF support. By

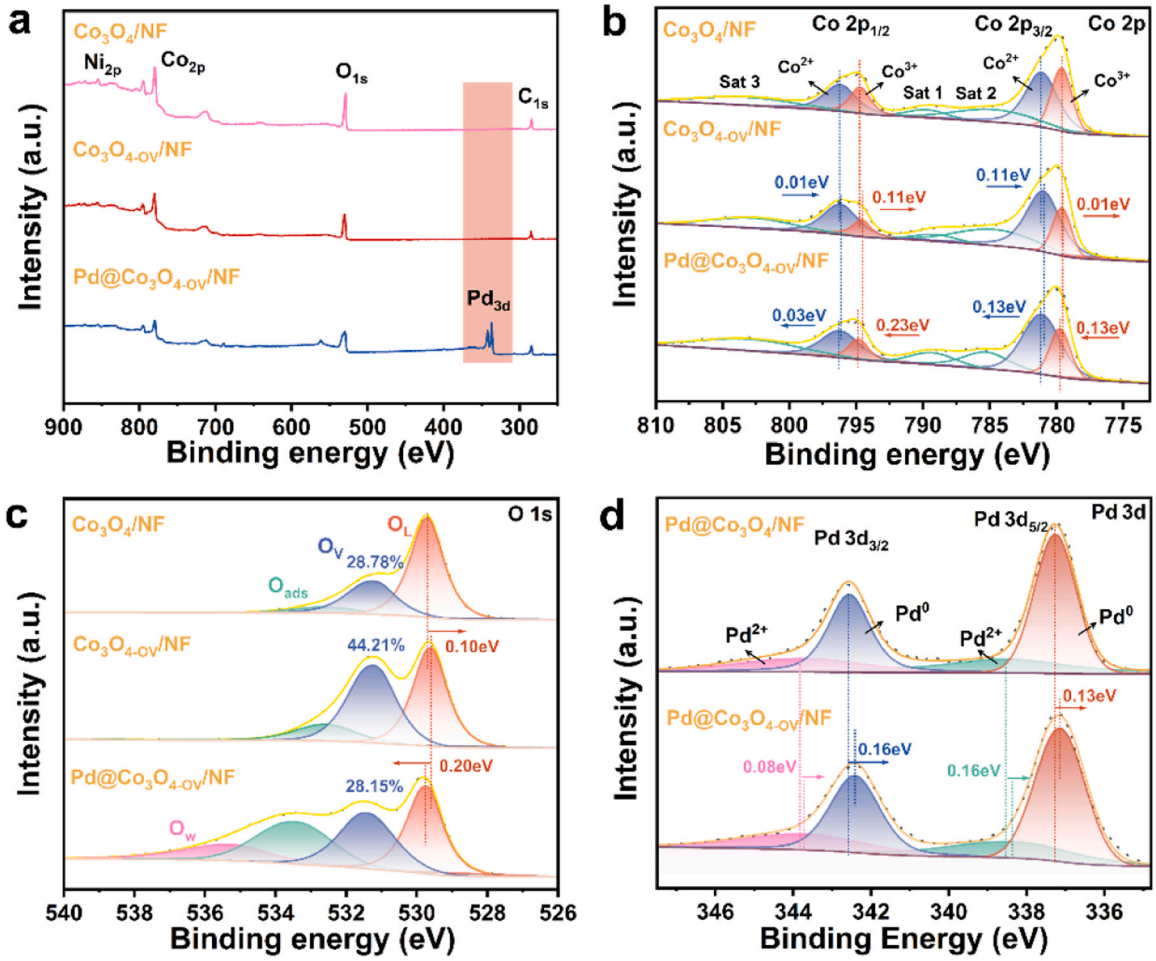

Fig. 2. XPS spectra of (a) the full elements, (b) Co 2p, and (c) O 1 s within Co_3O_4/NF, $Co_3O_{4\text{-}OV}$/NF, and Pd@$Co_3O_{4\text{-}OV}$/NF powder samples; (d) XPS spectra of Pd within Pd@Co_3O_4/NF and Pd@$Co_3O_{4\text{-}OV}$/NF powder samples.

analyzing the binding energy shift results of Co 2p, O_L, and Pd 3d, it is known that all of the above higher shifts of binding energies demonstrate a strong SMSI effect between $Co_3O_{4\text{-}OV}$ support and Pd, which leads to the transfer of electrons from $Co_3O_{4\text{-}OV}$ to Pd. According to prior studies, the EHDC reaction mechanism on Pd can be described as an indirect reduction process with the generated H* serving as an intermediary. It has been discovered that electron-rich Pd can promote the water dissociation process of H* generation in electrocatalysis. The trapped H_2O absorbs on electron-rich Pd and forms Pd-H* bonds by accepting the transferred electrons, hence promoting the H*-mediated EHDC reaction [47–49]. For electron-rich Pd, the Pd@$Co_3O_{4\text{-}OV}$/NF catalyst was expected to show good catalytic activity for 2,4-DCP.

3.2. Electrochemical catalytic performance

Linear sweep voltammetry (LSV) curves of different electrocatalysts in 0.05 M Na_2SO_4 solution were evaluated (Fig. 3a). The Co_3O_4/NF catalyst exhibits inferior performance characterised by a larger overpotential (-0.81 V at 10 mA cm^{-2}), suggesting its inherent inertness for water splitting. The introduction of oxygen vacancies for the Co_3O_4/NF enhances its performance and leads to a decrease in overpotential, as observed in the $Co_3O_{4\text{-}OV}$/NF catalyst with an overpotential of −0.75 V at a current density of 10 mA cm^{-2}. After Pd loading, the SMSI effect between Pd and $Co_3O_{4\text{-}OV}$/NF support further enhances the water activation ability of Pd@$Co_3O_{4\text{-}OV}$/NF (-0.70 V at 10 mA cm^{-2}). Fourier transform infrared (FT-IR) spectra reveal the promotion of O_V for water splitting (Fig. S7). The signal of O-H vibration peak of dissociative water at 3510 cm^{-1} of Pd@$Co_3O_{4\text{-}OV}$/NF is the strongest, indicating that Pd@$Co_3O_{4\text{-}OV}$/NF has a strong ability of water splitting [50]. The improved water splitting ability of the Pd@$Co_3O_{4\text{-}OV}$/NF electrocatalyst ensures a higher H* generation rate, which is conducive to the progress of the EHDC reaction. The generation of H* was strongly correlated with the applied potential. The recorded working potential on Pd@$Co_3O_{4\text{-}OV}$/NF and Pd@Co_3O_4/NF electrodes during the dechlorination process of 2,4-DCP can be observed in Fig. 3b. Under the influence of a consistent current of 10 mA cm^{-2}, the working potential of both electrodes exhibited two distinct stages. During the initial 10-minute period, there was a rapid decline in the working potentials of both systems, suggesting that the contents of adsorbed atomic H* were unstable. Between 10 and 130 minutes, the working potentials of Pd@$Co_3O_{4\text{-}OV}$/NF and Pd@Co_3O_4/NF exhibited a progressive incline, reaching around −0.71 and −0.70 V, respectively. These values corresponded to a current density of −8.0 and −9.7 mA cm^{-2} in Fig. 3a. Therefore, the working potentials on both electrocatalysts at a constant current of 10 mA cm^{-2} ensure the existence of sufficient H* to carry out the EHDC of 2,4-DCP, and the EHDC reaction will occur more rapidly on Pd@$Co_3O_{4\text{-}OV}$/NF [51]. The LSV curves of Pd@$Co_3O_{4\text{-}OV}$/NF in 0.05 M Na_2SO_4 solution (before and after adding 2,4-DCP) show the addition of 2,4-DCP leads to enhanced cathodic current density (Fig. S8), indicating that more H* will be consumed in EHDC [52]. All of the results indicate that the presence of $Co_3O_{4\text{-}OV}$ support would accelerate the Volmer reaction (water dissociation) and promote the generation of H*, resulting

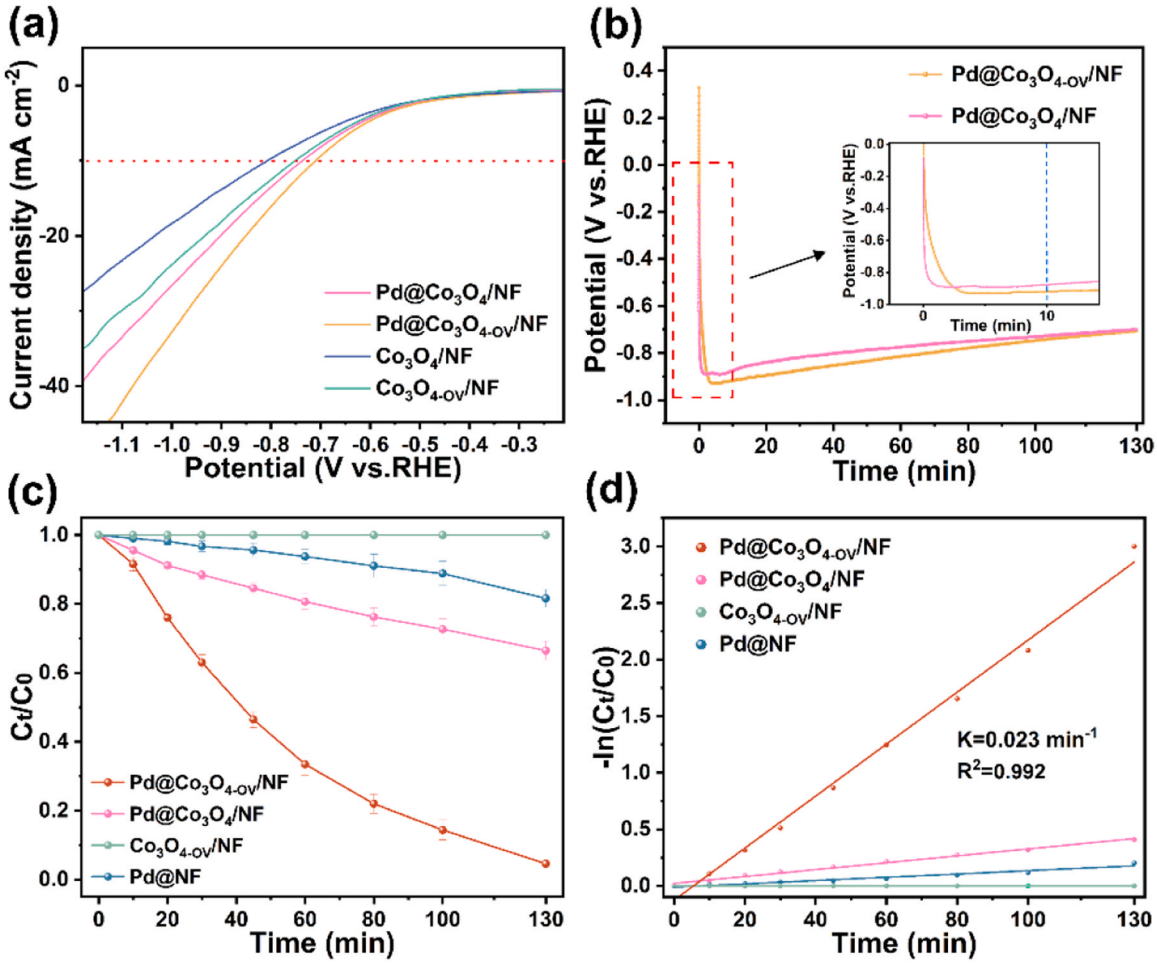

Fig. 3. (a) LSV curves of different electrocatalysts in 0.05 M Na_2SO_4 solution; (b) The working potential on Pd@$Co_3O_{4\text{-}OV}$/NF and Pd@Co_3O_4/NF electrodes during the electrochemical dechlorination of 2,4-DCP at a constant current of 10 mA cm^{-2}; (c) The time-dependent EHDC performances of 2,4-DCP (80 ppm) with different electrocatalysts; (d) The EHDC pseudo-first-order kinetic plots of 2,4-DCP (80 ppm) with different electrocatalysts.

in the enhanced EHDC activity of the Pd@$Co_3O_{4\text{-}OV}$/NF.

To evaluate the detox potential, the elimination efficiency of 2,4-DCP by the EHDC process with different electrocatalysts was examined. As shown in Fig. 3c, $Co_3O_{4\text{-}OV}$/NF can not effectively convert 2,4-DCP after electrolysis for 130 min since there is no active site on it. The EHDC of 2,4-DCP is substantially improved by the Pd@$Co_3O_{4\text{-}OV}$/NF with a 95.40% elimination efficiency after 130 min EHDC reaction, which is higher than Pd@Co_3O_4/NF (33.52%) and Pd@NF (18.38%). The EHDC kinetic was learned by using the pseudo-first-order kinetics model to intuitively analyze elimination efficacy of different electrocatalysts (Fig. 3d). The result shows that the EHDC kinetic of Pd@$Co_3O_{4\text{-}OV}$/NF is indicated to be fastest ($K = 0.023\ min^{-1}$) in all samples.

The impact of the starting 2,4-DCP concentration on the time-dependent performance during EHDC process using Pd@$Co_3O_{4\text{-}OV}$/NF is shown in Fig. 4a. The results indicate that Pd@$Co_3O_{4\text{-}OV}$/NF electrocatalyst exhibits favourable EHDC performance for low concentrations of 2,4-DCP. Fig. 4b compares the DA of Pd@$Co_3O_{4\text{-}OV}$/NF with that of most reported Pd-modified electrodes for EHDC of 2,4-DCP [16, 44, 52–56]. DA determined the amount (mmol) of 2.4-DCP treated with per unit mass (g) of Pd during per unit time. As shown in Fig. 4b, our catalyst has the highest DA for the EHDC of 2,4-DCP among different catalysts. Meanwhile, Pd@$Co_3O_{4\text{-}OV}$/NF has low Pd loading compared with other literatures reported, which indicates that the catalyst has a high Pd atoms utilization. The outcome demonstrates that Pd@$Co_3O_{4\text{-}OV}$/NF is competitive and superior to the majority of Pd-modified electrocatalysts reported to date. The time-dependent EHDC performances of different halogenated organic pollutants (80 ppm) were tested by using Pd@$Co_3O_{4\text{-}OV}$/NF electrode (Fig. 4c). Fig. 4d shows the related pseudo-first-order kinetic plots. The extremely strong C-F bond makes 2-Fluorophenol almost unconverted [57]. In contrast, 2-Chlorophenol, 4-Chlorophenol, and 2-Bromophenol are transformed rapidly in EHDC reaction, and the conversion efficiency of 2-Bromophenol is higher than that of 4-Chlorophenol and 2-Chlorophenol. Notably, the conversion efficacy of 4-chlorophenol is greater than that of 2-chlorophenol, which can be related to the difference that the Cl atom in the para-position of the hydroxyl group is more active than the one in the ortho-position [58]. The Pd@$Co_3O_{4\text{-}OV}$/NF electrocatalyst has good EHDC efficiency for 2,4-D, 2,4-DCBA, and CAP. The EHDC kinetic of CAP is indicated to be the fastest ($K = 0.034\ min^{-1}$) in all halogenated organic pollutants (Fig. 4d). In the case of significantly reducing the Pd loading, this Pd@$Co_3O_{4\text{-}OV}$/NF electrocatalyst shows high EHDC activity with a dechlorination activity of 1.79 $mmol_{2,4\text{-}D}\ g_{Pd}^{-1}\ min^{-1}$ for EHDC of 2,4-D, which is higher than that of the previous Pd-based EHDC electrocatalyst supported on Co_3O_4 (0.059 $mmol_{2,4\text{-}D}\ g_{Pd}^{-1}\ min^{-1}$) [59].

3.3. Stability and anti-interference ability

The adaptability of the electrode in the complex water environment is also a key indicator to measure the performance of electrocatalyst. The effectiveness of 2,4-DCP removal was evaluated in different pre-determined starting pH solutions. There is a volcanic relationship between EHDC efficiency and initial solution pH (Fig. 5a). The result shows that the Pd@$Co_3O_{4\text{-}OV}$/NF electrode has good EHDC efficiency in weakly acidic/alkaline water environment. The relative kinetic of EHDC

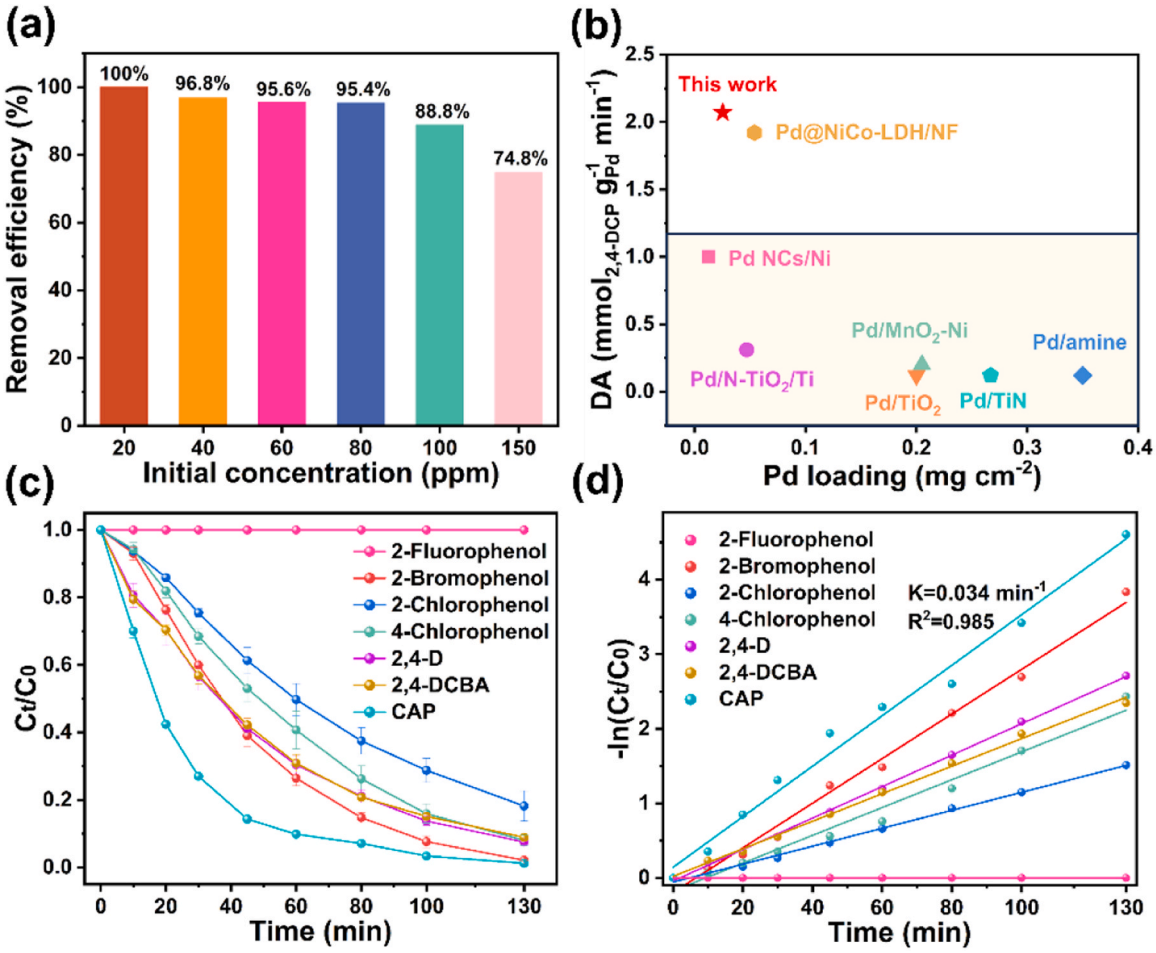

Fig. 4. (a) The effect of varying starting 2,4-DCP concentrations for EHDC on Pd@$Co_3O_{4\text{-}OV}$/NF; (b) Comparison of dechlorination activity (DA) between our electrocatalyst and most reported Pd modified electrocatalysts for EHDC of 2,4-DCP; (c-d) The time-dependent EHDC performances and the pseudo-first-order kinetic plots of different halogenated organic pollutants (80 ppm) dechlorination with Pd@$Co_3O_{4\text{-}OV}$/NF.

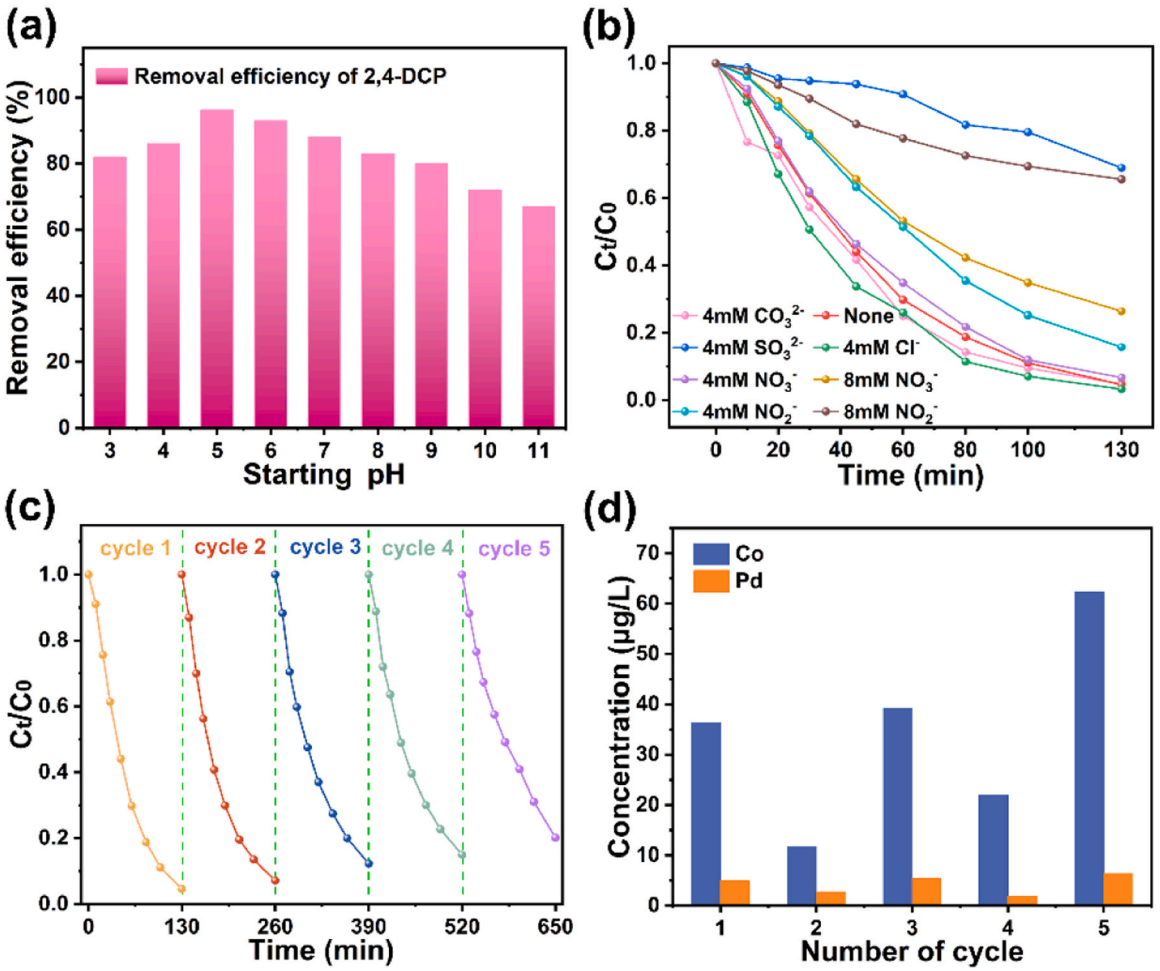

Fig. 5. (a) Elimination efficacy of 2,4-DCP in various specified initial pH solutions; (b) The effect of different dissolved anions on time-dependent EHDC performance of the Pd@$Co_3O_{4\text{-}OV}$/NF; (c-d) Elimination efficiency of 2,4-DCP during five successive EHDC runs and leaching concentration of Co and Pd on the Pd@$Co_3O_{4\text{-}OV}$/NF.

reaction can be adjusted by controlling the initial pH of solution.

Fig. S9 illustrates that pH of the solution steadily rises during the whole EHDC process in all systems. The change in solution pH during EHDC process is attributable to H* consumption. It is important to assess the influence of frequently encountered anions, including chloride (Cl^-), carbonate (CO_3^{2-}), nitrate (NO_3^-), nitrite (NO_2^-), and sulfite (SO_3^{2-}), present in water, on the efficacy of Pd@$Co_3O_{4\text{-}OV}$/NF in the EHDC process. This evaluation is important because these anions may potentially lead to active site poisoning or compete with H* species. The result in Fig. 5b clearly shows that except for SO_3^{2-}, NO_3^-, and NO_2^-, other anions (Cl^- and CO_3^{2-}) pose almost negligible effects on electrode performances. The impact of SO_3^{2-} (4 mM) on the elimination efficiency of 2,4-DCP is quite notable, as it achieves only a 31.04% removal rate. This outcome may be ascribed to the detrimental influence of SO_3^{2-} on the active Pd sites, mostly due to the formation of robust chemical bonds (S-Pd) [60]. The NO_3^- (4 mM) has a slight adverse impact, while the NO_3^- (8 mM), NO_2^- (4 mM), and NO_2^- (8 mM) have greater adverse effects on the removal efficiency of 2,4-DCP. This outcome might potentially be attributed to the cathodic reduction of H* species [61].

The stability of the EHDC performance of Pd@$Co_3O_{4\text{-}OV}$/NF electrocatalyst was evaluated (Fig. 5c). After undergoing five continuous EHDC process cycles, elimination efficacy of 2,4-DCP exhibited a reduction to 80.01%. The Pd and Co metals leaching of Pd@$Co_3O_{4\text{-}OV}$/NF were separately detected during five consecutive EHDC reaction cycles. Infinitesimal Co leaching and Pd leaching avoid generating secondary pollution (Fig. 5d). During the EHDC reaction, the tiny loss of Co and Pd within Pd@$Co_3O_{4\text{-}OV}$/NF electrode proves the SMSI positive effect and the structural stability of the electrocatalyst. The SEM of the Pd@$Co_3O_{4\text{-}OV}$/NF remained unchanged after EHDC reaction, indicating that the electrode has good structural stability (Fig. S10).

3.4. Toxicity assessment and reaction mechanism

The concentration evolutions of the reactant and intermediate during EHDC reaction on Pd@$Co_3O_{4\text{-}OV}$/NF were quantified. It can be seen that 2,4-DCP, o-CP, and P are found in system under investigation (Fig. 6a). However, no p-CP is discovered during EHDC process. This absence of p-CP may be attributed to the fact that the C-Cl bond in 2,4-DCP is more susceptible to cleavage in the para position compared to the adjacent position due to the steric hindrance effect [62]. The result shows the concentration of 2,4-DCP decreases fast, while that of phenol increases and o-CP remains low. It is noted that the total molar amount of benzene rings varies little throughout the EHDC reaction suggesting few side reactions and the high reaction selectivity for EHDC. A small amount of o-CP (a toxic persistent organic pollutant) still existed in the solution after the EHDC reaction, which may do some harm to the environment. The assessment of biosafety improvements in water was conducted by a comparative analysis of Chlorella cell activity in various solutions. The OD_{680} analysis results indicate that the density of Chlorella cells in the EHDC-treated solution is close to that of the control group and much greater than the untreated solution (Fig. 6b). The OD_{680} of Chlorella cells remained basically unchanged in the 2,4-DCP-contained solution, indicating that 2,4-DCP has the adverse effect of on Chlorella cells. The three digital images show that solution

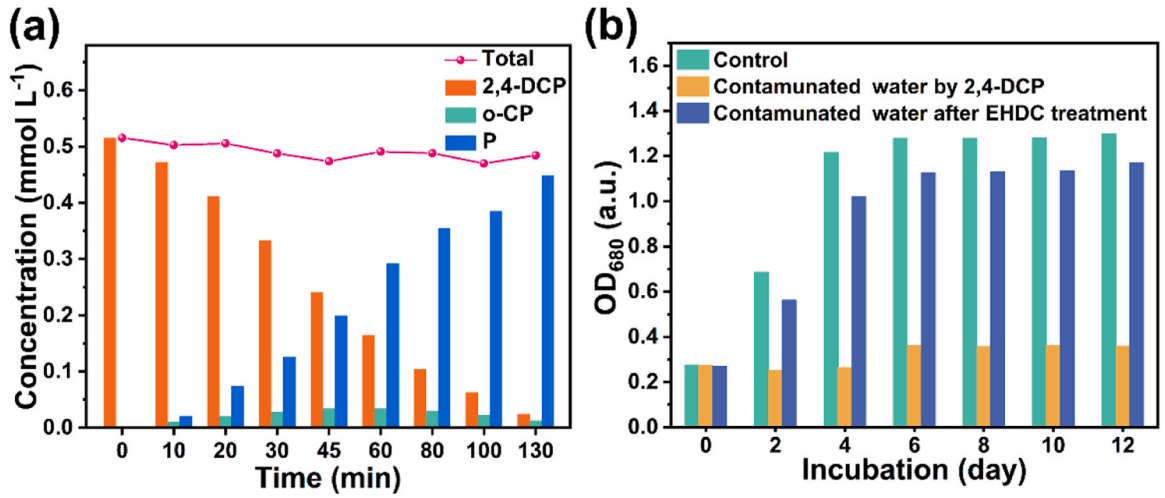

Fig. 6. (a) Concentration variations of the reactant, the reaction intermediate, and the final product throughout the EHDC process; (b) The evolution of OD_{680} of Chlorella cell solution during various incubation days.

contaminated 2,4-DCP exhibits yellow-green, which may be attributed to the loss of chlorophyll (Fig. S11) [63]. On the contrary, the solution treated with EHDC remains a similar green color to the control group. Therefore, it can be established that 2,4-DCP has an adverse effect on Chlorella cells, and the biosafety of water treated by EHDC has been improved.

During the EHDC process, indirect reductive dechlorination mediated by H* is the main pathway. To further study the indirect reduction mechanism on Pd@$Co_3O_{4\text{-}OV}$/NF, t-BuOH was added as an H* trapping agent. With the increase of t-BuOH concentration, the EHDC efficacy of 2,4-DCP on Pd@$Co_3O_{4\text{-}OV}$/NF is significantly inhibited (Fig. 7a). Furthermore, the ESR analysis by using DMPO as the probe reveals nine characteristic peaks of Pd@Co_3O_4/NF and Pd@$Co_3O_{4\text{-}OV}$/NF, corresponding to the existence of H* (Fig. 7b), a stronger peak intensity can be demonstrated as a higher concentration of H* [64–66]. The stronger signal of Pd@$Co_3O_{4\text{-}OV}$/NF confirms that H* formation has been enhanced. Fig. 7c depicts the promoted EHDC mechanism on Pd@$Co_3O_{4\text{-}OV}$/NF electrocatalyst for degradation of 2,4-DCP. The enhanced water splitting ability of Pd@$Co_3O_{4\text{-}OV}$/NF will boost H* production. Subsequently, the H* present on the Pd surface initiates the assault on the C-Cl bonds of 2,4-DCP, resulting in the conversion of 2,4-DCP into phenol. Finally, the phenol is desorbed from the catalyst.

4. Conclusions

In summary, oxygen vacancies-rich Co_3O_4 ($Co_3O_{4\text{-}OV}$) cone-like architecture growth in situ on Ni foam was used as an intermediate layer to obtain Pd@$Co_3O_{4\text{-}OV}$/NF composite electrode with low Pd loading (0.0254 mg cm^{-2}). The Pd of the catalyst, which has rich electrons, facilitates formation of H* through Pd-H bond, hence promoting EHDC reaction. The prepared Pd@$Co_3O_{4\text{-}OV}$/NF shows high EHDC activity with a dechlorination activity (DA) of 2.07 $mmol_{2,4\text{-}DCP}$ g_{Pd}^{-1} min^{-1} for EHDC of 2,4-DCP, which is higher than most reported Pd-modified electrodes. The Pd@$Co_3O_{4\text{-}OV}$/NF exhibited excellent anti-background interference ability (different initial pH and anions in aqueous solution) and good cycle stability (5 consecutive EHDC cycles), which could effectively improve aquatic biosafety in actual application. This study proposes a viable defect-regulating method for building EHDC electrocatalysts with fewer precious metals and quick electrocatalytic hydrodechlorination activity.

CRediT authorship contribution statement

Lipeng Diao: Data curation. **Maomao Liu:** Data curation. **Yuanyuan Sun:** Data curation. **Tao Li:** Writing – original draft. **Zhenyu Kong:** Methodology. **Dongjiang Yang:** Writing – review & editing. **Ping Lu:** Data curation. **Daohao Li:** Writing – review & editing.

Declaration of Competing Interest

The authors declare that they have no known competing financial interests or personal relationships that could have appeared to influence the work reported in this paper.

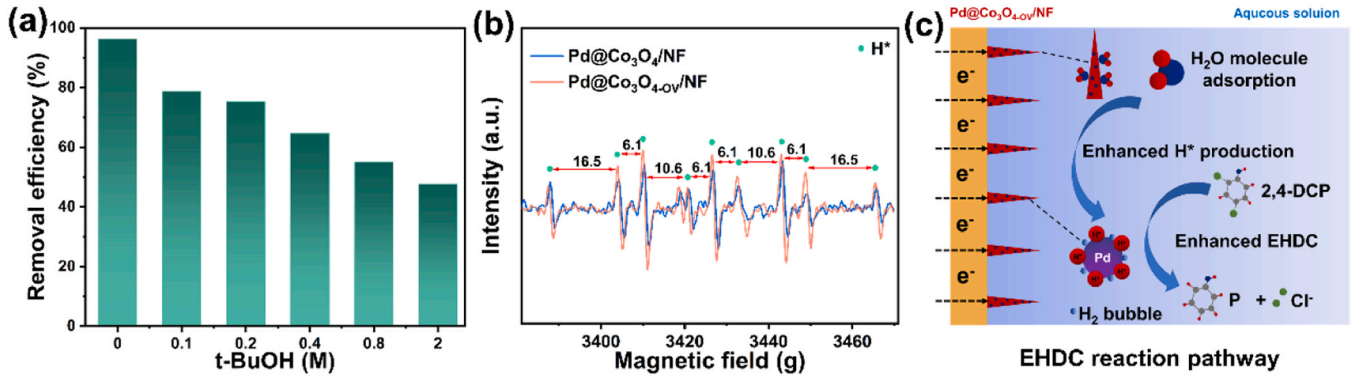

Fig. 7. (a) EHDC performance of 2,4-DCP on Pd@$Co_3O_{4\text{-}OV}$/NF under different t-BuOH concentrations; (b) The DMPO spin-trapping ESR spectra of Pd@Co_3O_4/NF and Pd@$Co_3O_{4\text{-}OV}$/NF; (c) The EHDC reaction pathway on Pd@$Co_3O_{4\text{-}OV}$/NF.

Data Availability

Data will be made available on request.

Acknowledgements

This work acknowledges the National Natural Science Foundation of China (Nos. 52302272 and 2376110), the Taishan Scholars Program (Nos. tsqn202211124 and ts201712030), the Natural Science Foundation of Shandong Province (No. ZR2022QB023), the Qingchuang Talents Induction Program of Shandong Higher Education Institution (Research and Innovation Team of Marine Polysaccharides Fibers-based Energy Materials), and the State Key Laboratory of Bio-Fibers and Eco-Textiles, Qingdao University (Nos. ZKT10 and GZRC202006).

Appendix A. Supporting information

Supplementary data associated with this article can be found in the online version at doi:10.1016/j.apcatb.2024.123968.

References

[1] M.Á. Arellano-González, I. González, A.-C. Texier, Mineralization of 2-chlorophenol by sequential electrochemical reductive dechlorination and biological processes, J. Hazard. Mater. 314 (2016) 181–187, https://doi.org/10.1016/j.jhazmat.2016.04.048.

[2] J. Li, Y. Wang, B. Zhao, J. Ding, J. Zhang, M. Yin, Z. Zhang, S. Ma, Y. Liu, Z. Tan, H. Zhang, L. Wang, D.D. Dionysiou, Unraveling kinetics and mechanism of electrocatalytic hydrodechlorination of chlorinated PPCPs by nickel-cobalt metal organic framework supported palladium composite electrode, Appl. Catal. B-Environ. 332 (2023) 122754, https://doi.org/10.1016/j.apcatb.2023.122754.

[3] J. Nieto-Sandoval, E. Gomez-Herrero, M. Munoz, Z.M. de Pedro, J.A. Casas, Palladium-based catalytic membrane reactor for the continuous flow hydrodechlorination of chlorinated micropollutants, Appl. Catal. B-Environ. 293 (2021) 120235, https://doi.org/10.1016/j.apcatb.2021.120235.

[4] Z. He, Q. Jian, J. Tang, T. Xu, J. Xu, Z. Yu, J. Chen, S. Song, Improvement of electrochemical reductive dechlorination of 2,4-dichlorophenoxyacetic acid using palladium catalysts prepared by a pulsed electrodeposition method, Electrochim. Acta 222 (2016) 488–498, https://doi.org/10.1016/j.electacta.2016.11.001.

[5] J. Jesus, D. Frascari, T. Pozdniakova, A.S. Danko, Kinetics of aerobic cometabolic biodegradation of chlorinated and brominated aliphatic hydrocarbons: a review, J. Hazard. Mater. 309 (2016) 37–52, https://doi.org/10.1016/j.jhazmat.2016.01.065.

[6] T.P. Needham, R.B. Payne, K.R. Sowers, U. Ghosh, Kinetics of PCB microbial dechlorination explained by freely dissolved concentration in sediment microcosms, Environ. Sci. Technol. 53 (2019) 7432–7441, https://doi.org/10.1021/acs.est.9b01088.

[7] J. Jiang, X. Zhang, X. Zhu, Y. Li, Removal of Intermediate aromatic halogenated DBPs by activated carbon adsorption: a new approach to controlling halogenated DBPs in chlorinated drinking water, Environ. Sci. Technol. 51 (2017) 3435–3444, https://doi.org/10.1021/acs.est.6b06161.

[8] Q.-S. Huang, C. Wang, W. Wei, B.-J. Ni, Magnetic poly(aniline-co-5-sulfo-2-anisidine) as multifunctional adsorbent for highly effective co-removal of aqueous Cr(VI) and 2,4-Dichlophenol, Chem. Eng. J. 387 (2020) 124152, https://doi.org/10.1016/j.cej.2020.124152.

[9] J. Ma, K. Wang, C. Wang, X. Chen, W. Zhu, G. Zhu, W. Yao, Y. Zhu, Photocatalysis-self-Fenton system with high-fluent degradation and high mineralization ability, Appl. Catal. B-Environ. 276 (2020) 119150, https://doi.org/10.1016/j.apcatb.2020.119150.

[10] Q. You, C. Zhang, M. Cao, B. Wang, J. Huang, Y. Wang, S. Deng, G. Yu, Defects controlling, elements doping, and crystallinity improving triple-strategy modified carbon nitride for efficient photocatalytic diclofenac degradation and H_2O_2 production, Appl. Catal. B-Environ. 321 (2023) 121941, https://doi.org/10.1016/j.apcatb.2022.121941.

[11] Y. Chen, C. Feng, W. Wang, Z. Liu, J. Li, C. Liu, Y. Pan, Y. Liu, Electronic structure engineering of bimetallic Pd-Au alloy nanocatalysts for improving electrocatalytic hydrodechlorination performance, Sep. Purif. Technol. 289 (2022) 120731, https://doi.org/10.1016/j.seppur.2022.120731.

[12] J. Li, S. Ma, Z. Qi, J. Ding, M. Yin, B. Zhao, Z. Zhang, Y. Wang, H. Zhang, L. Wang, D.D. Dionysiou, Insights into the removal of chloramphenicol by electrochemical reduction on Pd/NiFe-MOF/foam-Ni electrode: performance and mechanism, Appl. Catal. B-Environ. 322 (2023) 122076, https://doi.org/10.1016/j.apcatb.2022.122076.

[13] Y. Shen, Y. Tong, J. Xu, S. Wang, J. Wang, T. Zeng, Z. He, W. Yang, S. Song, Ni-based layered metal-organic frameworks with palladium for electrochemical dechlorination, Appl. Catal. B-Environ. 264 (2020) 118505, https://doi.org/10.1016/j.apcatb.2019.11850.

[14] Y. Wu, L. Gan, S. Zhang, H. Song, C. Lu, W. Li, Z. Wang, B. Jiang, A. Li, Carbon-nanotube-doped Pd-Ni bimetallic three-dimensional electrode for electrocatalytic hydrodechlorination of 4-chlorophenol: enhanced activity and stability, J. Hazard. Mater. 356 (2018) 17–25, https://doi.org/10.1016/j.jhazmat.2018.05.034.

[15] Z. Lou, J. Xu, J. Zhou, K. Yang, Z. Cao, Y. Li, Y. Liu, L. Lou, X. Xu, Insight into atomic H* generation, H_2 evolution, and cathode potential of MnO_2 induced Pd/Ni foam cathode for electrocatalytic hydrodechlorination, Chem. Eng. J. 374 (2019) 211–220, https://doi.org/10.1016/j.cej.2019.05.171.

[16] J. Wang, X. Wei, P. Wang, J. Miao, R. Zhang, N. Zhang, X. Zhou, H. Xu, J. Zhang, H. Li, S. Peng, Insights into the enhanced performance of NiCo-LDH modified Pd/NF cathode for electrocatalytic hydrodechlorination, Fuel 341 (2023) 127689, https://doi.org/10.1016/j.fuel.2023.127689.

[17] J. Zhou, Z. Lou, K. Yang, J. Xu, Y. Li, Y. Liu, S.A. Baig, X. Xu, Electrocatalytic dechlorination of 2,4-dichlorobenzoic acid using different carbon-supported palladium moveable catalysts: adsorption and dechlorination activity, Appl. Catal. B-Environ. 244 (2019) 215–224, https://doi.org/10.1016/j.apcatb.2018.11.052.

[18] Z. Lou, Y. Li, J. Zhou, K. Yang, Y. Liu, S.A. Baig, X. Xu, TiC doped palladium/nickel foam cathode for electrocatalytic hydrodechlorination of 2,4-DCBA: enhanced electrical conductivity and reactive activity, J. Hazard. Mater. 362 (2019) 148–159, https://doi.org/10.1016/j.jhazmat.2018.08.066.

[19] K. Zhang, G. Zhang, J. Qu, H. Liu, Disordering the Atomic Structure of Co(II) Oxide via B-Doping: an efficient oxygen vacancy introduction approach for high oxygen evolution reaction electrocatalysts, Small 14 (2018) 1802760, https://doi.org/10.1002/smll.201802760.

[20] Y. Xu, K. Fan, Y. Zou, H. Fu, M. Dong, Y. Dou, Y. Wang, S. Chen, H. Yin, M. Al-Mamun, P. Liu, H. Zhao, Rational design of metal oxide catalysts for electrocatalytic water splitting, Nanoscale 13 (2021) 20324–20353, https://doi.org/10.1039/D1NR06285A.

[21] Z. Wu, Y. Zhao, W. Jin, B. Jia, J. Wang, T. Ma, Recent progress of vacancy engineering for electrochemical energy conversion related applications, Adv. Funct. Mater. 31 (2021) 2009070, https://doi.org/10.1002/adfm.202009070.

[22] G. Zhuang, Y. Chen, Z. Zhuang, Y. Yu, J. Yu, Oxygen vacancies in metal oxides: recent progress towards advanced catalyst design, Sci. China-Mater. 63 (2020) 2089–2118, https://doi.org/10.1007/s40843-020-1305-6.

[23] L. Zhuang, Y. Jia, H. Liu, X. Wang, R.K. Hocking, H. Liu, J. Chen, L. Ge, L. Zhang, M. Li, C.-L. Dong, Y.-C. Huang, S. Shen, D. Yang, Z. Zhu, X. Yao, Defect-induced Pt–Co–Se coordinated sites with highly asymmetrical electronic distribution for boosting oxygen-involving electrocatalysis, Adv. Mater. 31 (2019) 1805581, https://doi.org/10.1002/adma.201805581.

[24] Z. Luo, G. Zhao, H. Pan, W. Sun, Strong metal–support interaction in heterogeneous catalysts, Adv. Energy Mater. 12 (2022) 2201395, https://doi.org/10.1002/aenm.202201395.

[25] Y. Wang, T. Zhou, K. Jiang, P. Da, Z. Peng, J. Tang, B. Kong, W.-B. Cai, Z. Yang, G. Zheng, Reduced mesoporous Co_3O_4 nanowires as efficient water oxidation electrocatalysts and supercapacitor electrodes, Adv. Energy Mater. 4 (2014) 1400696, https://doi.org/10.1002/aenm.201400696.

[26] P. Liu, Y. Zhao, R. Qin, S. Mo, G. Chen, L. Gu, D.M. Chevrier, P. Zhang, Q. Guo, D. Zang, B. Wu, G. Fu, N. Zheng, Photochemical route for synthesizing atomically dispersed palladium catalysts, Science 352 (2016) 797–800, https://doi.org/10.1126/science.aaf5251.

[27] H. Wei, H. Wu, K. Huang, B. Ge, J. Ma, J. Lang, D. Zu, M. Lei, Y. Yao, W. Guo, H. Wu, Ultralow-temperature photochemical synthesis of atomically dispersed Pt catalysts for the hydrogen evolution reaction, Chem. Sci. 10 (2019) 2830–2836, https://doi.org/10.1039/C8SC04986F.

[28] H. Chen, M. Yang, S. Tao, G. Chen, Oxygen vacancy enhanced catalytic activity of reduced Co_3O_4 towards p-nitrophenol reduction, Appl. Catal. B-Environ. 209 (2017) 648–656, https://doi.org/10.1016/j.apcatb.2017.03.038.

[29] Y. Liu, L. Liu, J. Shan, J. Zhang, Electrodeposition of palladium and reduced graphene oxide nanocomposites on foam-nickel electrode for electrocatalytic hydrodechlorination of 4-chlorophenol, J. Hazard. Mater. 290 (2015) 1–8, https://doi.org/10.1016/j.jhazmat.2015.02.016.

[30] J. Liu, J. Ke, Y. Li, B. Liu, L. Wang, H. Xiao, S. Wang, Co_3O_4 quantum dots/TiO_2 nanobelt hybrids for highly efficient photocatalytic overall water splitting, Appl. Catal. B-Environ. 236 (2018) 396–403, https://doi.org/10.1016/j.apcatb.2018.05.042.

[31] X. Zhou, Z. Liu, Y. Wang, Y. Ding, Facet effect of Co_3O_4 nanocrystals on visible-light driven water oxidation, Appl. Catal. B-Environ. 237 (2018) 74–84, https://doi.org/10.1016/j.apcatb.2018.05.067.

[32] Z. Lou, C. Yu, X. Wen, Y. Xu, J. Yu, X. Xu, Construction of Pd nanoparticles/two-dimensional Co-MOF nanosheets heterojunction for enhanced electrocatalytic hydrodechlorination, Appl. Catal. B-Environ. 317 (2022) 121730, https://doi.org/10.1016/j.apcatb.2022.121730.

[33] W. Jiang, B. Xu, Z. Xiang, X. Liu, F. Liu, Preparation and reactivity of UV light-reduced Pd/α-Fe_2O_3 catalyst towards the hydrogenation of *o*-chloronitrobenzene, Appl. Catal. A-Gen. 520 (2016) 65–72, https://doi.org/10.1016/j.apcata.2016.04.007.

[34] C. Chen, L. Jin, H. Dong, J. Jiang, H. Feng, D. Chen, N. Li, Q. Xu, J. Lu, Modulating adsorption of active hydrogen atoms on palladium nanoparticles: doping ruthenium into metal–organic frameworks for efficient electrocatalytic hydrodechlorination, Sep. Purif. Technol. 324 (2023) 124527, https://doi.org/10.1016/j.seppur.2023.124527.

[35] T. Zhang, S. Zhao, C. Zhu, J. Shi, C. Su, J. Yang, M. Wang, J. Li, J. Li, P. Liu, C. Wang, Rational construction of high-active Co_3O_4 electrocatalysts for oxygen evolution reaction, Nano Res. 16 (2023) 624–633, https://doi.org/10.1007/s12274-022-4879-2.

[36] Y.P. Zhu, T.Y. Ma, M. Jaroniec, S.Z. Qiao, Self-templating synthesis of hollow Co_3O_4 microtube arrays for highly efficient water electrolysis, Angew. Chem. Int. Ed. 56 (2017) 1324–1328, https://doi.org/10.1002/anie.201610413.

[37] H. Sun, Y. Zhao, K. Mølhave, M. Zhang, J. Zhang, Simultaneous modulation of surface composition, oxygen vacancies and assembly in hierarchical Co_3O_4 mesoporous nanostructures for lithium storage and electrocatalytic oxygen evolution, Nanoscale 9 (2017) 14431–14441, https://doi.org/10.1039/C7NR03810K.
[38] Y. Qi, X. Xiao, Y. Mei, L. Xiong, L. Chen, X. Lin, Z. Lin, S. Sun, B. Han, D. Yang, Y. Qin, X. Qiu, Modulation of brønsted and lewis acid centers for $Ni_xCo_{3-x}O_4$ spinel catalysts: towards efficient catalytic conversion of lignin, Adv. Funct. Mater. 32 (2022) 2111615, https://doi.org/10.1002/adfm.202111615.
[39] S. Guo, J. Wang, Y. Sun, L. Peng, C. Li, Interface engineering of Co_3O_4/CeO_2 heterostructure in-situ embedded in Co/N-doped carbon nanofibers integrating oxygen vacancies as effective oxygen cathode catalyst for Li-O_2 battery, Chem. Eng. J. 452 (2023) 139317, https://doi.org/10.1016/j.cej.2022.139317.
[40] Z. Cai, Y. Bi, E. Hu, W. Liu, N. Dwarica, Y. Tian, X. Li, Y. Kuang, Y. Li, X.-Q. Yang, H. Wang, X. Sun, Single-crystalline ultrathin Co_3O_4 nanosheets with massive vacancy defects for enhanced electrocatalysis, Adv. Energy Mater. 8 (2018) 1701694, https://doi.org/10.1002/aenm.201701694.
[41] J. Ji, C. Zhang, X. Yang, F. Kong, C. Wu, H. Duan, D. Yang, Pt-stabilized electron-rich Ir structures for low temperature methane combustion with enhanced sulfur-resistance, Chem. Eng. J. 466 (2023) 143044, https://doi.org/10.1016/j.cej.2023.143044.
[42] H. He, J. Chen, D. Zhang, F. Li, X. Chen, Y. Chen, L. Bian, Q. Wang, P. Duan, Z. Wen, X. Lv, Modulating the electrocatalytic performance of Palladium with the electronic metal–support interaction: a case study on oxygen evolution reaction, ACS Catal. 8 (2018) 6617–6626, https://doi.org/10.1021/acscatal.8b00460.
[43] R. Wei, M. Fang, G. Dong, C. Lan, L. Shu, H. Zhang, X. Bu, J.C. Ho, High-Index faceted porous Co_3O_4 nanosheets with oxygen vacancies for highly efficient water oxidation, ACS Appl. Mater. Interfaces 10 (2018) 7079–7086, https://doi.org/10.1021/acsami.7b18208.
[44] J. Li, Y. Peng, W. Zhang, X. Shi, M. Chen, P. Wang, X. Zhang, H. Fu, X. Lv, F. Dong, G. Jiang, Hierarchical Pd/MnO_2 nanosheet array supported on Ni foam: an advanced electrode for electrocatalytic hydrodechlorination reaction, Appl. Surf. Sci. 509 (2020) 145369, https://doi.org/10.1016/j.apsusc.2020.145369.
[45] H. Chen, Z. Yang, X. Wang, F. Polo-Garzon, P.W. Halstenberg, T. Wang, X. Suo, S.-Z. Yang, H.M. Meyer III, Z. Wu, S. Dai, Photoinduced strong metal–support interaction for enhanced catalysis, J. Am. Chem. Soc. 143 (2021) 8521–8526, https://doi.org/10.1021/jacs.0c12817.
[46] L. Liu, G. Liu, S. Niu, H. Liu, M. Cui, A. Wang, Atomic hydrogen-mediated enhanced electrocatalytic hydrodehalogenation on Pd@MXene electrodes, J. Hazard. Mater. 459 (2023) 132113, https://doi.org/10.1016/j.jhazmat.2023.132113.
[47] Z. Zhao, L. Yu, L. Zheng, T. Guo, Z. Lv, S. Song, H. Zheng, TiO_2@PDA inorganic-organic core-shell skeleton supported Pd nanodots for enhanced electrocatalytic hydrodechlorination, J. Hazard. Mater. 435 (2022) 128998, https://doi.org/10.1016/j.jhazmat.2022.128998.
[48] S. Hong, K. Ham, J. Hwang, S. Kang, M.H. Seo, Y.-W. Choi, B. Han, J. Lee, K. Cho, Active motif change of Ni-Fe spinel oxide by Ir doping for highly durable and facile oxygen evolution reaction, Adv. Funct. Mater. 33 (2023) 2209543, https://doi.org/10.1002/adfm.202209543.
[49] J. Li, K. Kong, Y. Chong, J. Ding, L. Wang, Z. Ba, J. Zhang, Unveiling the mechanism and performance of electrocatalytic hydrodechlorination of chlorinated PPCPs by electron-rich palladium electrode modulated through PANI-rGO interlayer, Sep. Purif. Technol. 323 (2023) 124452, https://doi.org/10.1016/j.seppur.2023.124452.
[50] Y. Liu, H.T.D. Bui, A.R. Jadhav, T. Yang, S. Saqlain, Y. Luo, J. Yu, A. Kumar, H. Wang, L. Wang, V.Q. Bui, M.G. Kim, Y.D. Kim, H. Lee, Revealing the synergy of cation and anion vacancies on improving overall water splitting kinetics, Adv. Funct. Mater. 31 (2021) 2010718, https://doi.org/10.1002/adfm.202010718.
[51] Z. Lou, J. Zhou, M. Sun, J. Xu, K. Yang, D. Lv, Y. Zhao, X. Xu, MnO_2 enhances electrocatalytic hydrodechlorination by Pd/Ni foam electrodes and reduces Pd needs, Chem. Eng. J. 352 (2018) 549–557, https://doi.org/10.1016/j.cej.2018.07.057.
[52] H. Wu, Z. Mao, B. Liu, D. Chen, M. Shi, B. Lv, Y. Xu, L. Wang, Ultra-low-loading Pd nanocrystals modified Ni foam electrode for efficient electrochemical hydrodechlorination, Appl. Catal. B-Environ. 337 (2023) 122978, https://doi.org/10.1016/j.apcatb.2023.122978.
[53] X. Wei, J. Wang, J. Miao, R. Zhang, W. Lu, N. Zhang, X. Zhou, H. Xu, J. Zhang, S. Peng, Enhanced performance of an in-situ synthesized Pd/N-TiO_2/Ti cathode for electrocatalytic hydrodechlorination, Colloid Surf. A-Physicochem. Eng. Asp. 648 (2022) 129320, https://doi.org/10.1016/j.colsurfa.2022.129320.
[54] K. Wang, S. Shu, M. Chen, J. Li, K. Zhou, J. Pan, X. Wang, X. Li, J. Sheng, F. Dong, G. Jiang, Pd-TiO_2 Schottky heterojunction catalyst boost the electrocatalytic hydrodechlorination reaction, Chem. Eng. J. 381 (2020) 122673, https://doi.org/10.1016/j.cej.2019.122673.
[55] W. Fu, S. Shu, J. Li, X. Shi, X. Lv, Y.-X. Huang, F. Dong, G. Jiang, Identifying the rate-determining step of the electrocatalytic hydrodechlorination reaction on palladium nanoparticles, Nanoscale 11 (2019) 15892–15899, https://doi.org/10.1039/C9NR04634H.
[56] G. Jiang, X. Shi, M. Cui, W. Wang, P. Wang, G. Johnson, Y. Nie, X. Lv, X. Zhang, F. Dong, S. Zhang, Surface ligand environment boosts the electrocatalytic hydrodechlorination reaction on Palladium nanoparticles, ACS Appl. Mater. Interfaces 13 (2021) 4072–4083, https://doi.org/10.1021/acsami.0c20994.
[57] O. Eisenstein, J. Milani, R.N. Perutz, Selectivity of C–H activation and competition between C–H and C–F bond activation at fluorocarbons, Chem. Rev. 117 (2017) 8710–8753, https://doi.org/10.1021/acs.chemrev.7b00163.
[58] Y. Guo, Y. Li, Z. Wang, Electrocatalytic hydro-dehalogenation of halogenated organic pollutants from wastewater: A critical review, Water Res 234 (2023) 119810, https://doi.org/10.1016/j.watres.2023.119810.
[59] Q. Liu, Y. Shen, S. Song, Z. He, Enhanced electrocatalytic hydrodechlorination of 2,4-dichlorophenoxyacetic acid by a Pd-Co_3O_4/Ni foam electrode, RSC Adv. 9 (2019) 12124–12133, https://doi.org/10.1039/C9RA01843C.
[60] J. Li, Y. Chen, R. Bai, C. Chen, W. Wang, Y. Pan, Y. Liu, Construction of Pd/Ni_2P-Ni foam nanosheet array electrode by in-situ phosphatization-electrodeposition strategy for synergistic electrocatalytic hydrodechlorination, Chem. Eng. J. 435 (2022) 134932, https://doi.org/10.1016/j.cej.2022.134932.
[61] M. Chen, S. Shu, J. Li, X. Lv, F. Dong, G. Jiang, Activating palladium nanoparticles via a Mott-Schottky heterojunction in electrocatalytic hydrodechlorination reaction, J. Hazard. Mater. 389 (2020) 121876, https://doi.org/10.1016/j.jhazmat.2019.121876.
[62] W. Yu, H. Jiang, J. Fang, S. Song, Designing an electron-deficient Pd/$NiCo_2O_4$ bifunctional electrocatalyst with an enhanced hydrodechlorination activity to reduce the consumption of Pd, Environ. Sci. Technol. 55 (2021) 10087–10096, https://doi.org/10.1021/acs.est.1c01922.
[63] K. Jiang, X. Shi, M. Chen, X. Lv, H. Gong, Y. Shen, P. Wang, F. Dong, M. Liu, X. Zhang, G. Jiang, Optimizing the metal-support interactions at the Pd-polymer carbon nitride Mott-Schottky heterojunction interface for an enhanced electrocatalytic hydrodechlorination reaction, J. Hazard. Mater. 411 (2021) 125119, https://doi.org/10.1016/j.jhazmat.2021.125119.
[64] H. Liu, J. Han, J. Yuan, C. Liu, D. Wang, T. Liu, M. Liu, J. Luo, A. Wang, J. C. Crittenden, Deep Dehalogenation of florfenicol using crystalline CoP nanosheet arrays on a Ti plate via direct cathodic reduction and atomic H, Environ. Sci. Technol. 53 (2019) 11932–11940, https://doi.org/10.1021/acs.est.9b04352.
[65] Z. Lou, C. Yu, X. Wen, Y. Xu, J. Yu, X. Xu, Construction of Pd nanoparticles/two-dimensional Co-MOF nanosheets heterojunction for enhanced electrocatalytic hydrodechlorination, Appl. Catal. B-Environ. 317 (2022) 121730, https://doi.org/10.1016/j.apcatb.2022.121730.
[66] Z. Fan, H. Zhao, K. Wang, W. Ran, J.-F. Sun, J. Liu, R. Liu, Enhancing electrocatalytic hydrodechlorination through interfacial microenvironment modulation, Environ. Sci. Technol. 57 (2023) 1499–1509, https://doi.org/10.1021/acs.est.2c07462.